

The simulation of turbulent particle-laden channel flow by the Lattice Boltzmann method

Amir Banari^{1,2,*,†}, Yackar Mauzole³, Tetsu Hara³, Stephan T. Grilli¹ and Christian F. Janßen²

¹*Department of Ocean Engineering, University of Rhode Island, USA*

²*Institute for Fluid Dynamics and Ship Theory, Hamburg University of Technology, Germany*

³*Graduate School of Oceanography, University of Rhode Island, USA*

SUMMARY

We perform direct numerical simulation of three-dimensional turbulent flows in a rectangular channel, with a lattice Boltzmann method, efficiently implemented on heavily parallel general purpose graphical processor units. After validating the method for a single fluid, for standard boundary layer problems, we study changes in mean and turbulent properties of particle-laden flows, as a function of particle size and concentration. The problem of physical interest for this application is the effect of water droplets on the turbulent properties of a high-speed air flow, near a solid surface. To do so, we use a Lagrangian tracking approach for a large number of rigid spherical point particles, whose motion is forced by drag forces caused by the fluid flow; particle effects on the latter are in turn represented by distributed volume forces in the lattice Boltzmann method. Results suggest that, while mean flow properties are only slightly affected, unless a very large concentration of particles is used, the turbulent vortices present near the boundary are significantly damped and broken down by the turbulent motion of the heavy particles, and both turbulent Reynolds stresses and the production of turbulent kinetic energy are decreased because of the particle effects. We also find that the streamwise component of turbulent velocity fluctuations is increased, while the spanwise and wall-normal components are decreased, as compared with the single fluid channel case. Additionally, the streamwise velocity of the carrier (air) phase is slightly reduced in the logarithmic boundary layer near the solid walls. Copyright © 2015 John Wiley & Sons, Ltd.

Received 11 September 2014; Revised 11 May 2015; Accepted 25 May 2015

KEY WORDS: lattice Boltzmann method; turbulent channel flow; Lagrangian point particle tracking; GPGPU implementation

1. INTRODUCTION

The study of turbulent particle-laden flows is important for various fluid mechanics problems of scientific and practical interest. Such flows frequently occur in nature and in industrial applications, for example, as a result of the release of sea sprays in the lower atmospheric turbulent boundary layer above the ocean, or in the scope of pollutants in the atmosphere and the ocean, chemical and oil engineering, and in sedimentation problems. Although turbulent particle-laden flows have been extensively studied in the past two decades, the full understanding of the modifications they induce to turbulent flow properties is still lacking. The complexity of such fluid flows and the numerous governing parameters that must be considered in their numerical simulations make it a challenging problem of which many aspects are still poorly understood and thus actively researched.

*Correspondence to: Amir Banari, Institute for Fluid Dynamics and Ship Theory, Hamburg University of Technology, Schwarzenbergstrasse 95C, 21073 Hamburg Room C5.017, Germany.

†E-mail: amir.banari@tuhh.de

The behavior of dispersed multiphase flows can be classified according to the level of interactions between the carrier (fluid) and the dispersed (particle) phases. Elghobashi [1] represented the different interactions that can be observed in such flows in terms of two parameters: (i) the particle Stokes number St , which is the particle response time τ_p , a measure of the particle inertia, normalized by the turbulence time scale τ_e or the Kolmogorov time scale $\tau_K = \sqrt{\nu/\varepsilon}$ (where ν is the fluid kinematic viscosity and ε the rate of dissipation of turbulent kinetic energy (TKE)) and (ii) the particle volume fraction Φ_{pv} . When $\Phi_{pv} < 10^{-6}$, the flow governs the particle trajectories, but the dispersed phase has a negligible effect on flow turbulence. In this case, the interactions between the two phases are unidirectional only, that is, a *one-way coupling* from fluid to particles exists. For intermediate volume fractions, $10^{-6} \leq \Phi_{pv} \leq 10^{-3}$, the momentum transfer from the particles to the flow turbulence is large enough to alter the turbulent structures [1]: this is a case where the interactions between the two phases are bidirectional, and the coupling is referred to as *two-way coupling* (i.e., from fluid to particles and from particles to fluid). In the case of very dense suspensions, for $\Phi_{pv} > 10^{-3}$, strong interactions (i.e., collisions) between particles become important, and the coupling is called a *four-way coupling* (i.e., between carrier fluid and particles and among the particles). While one-way and two-way coupled systems have been extensively investigated, both numerically and experimentally [2], the four-way coupling implies that the dynamics of droplets, such as breakup or coalescence, have to be taken into account, which represents a much larger computational challenge.

In the following, we discuss some of the key findings of earlier work performed for moderately dense suspensions. Rashidi *et al.* [3] experimentally studied the wall turbulence with polystyrene particle of various sizes. Results showed that the larger particles enhance Reynolds shear stresses and also increase the number of wall ejections, while the smaller particles lead to opposite effects on the turbulent fields. Squires and Eaton [4], in their two-way coupled direct numerical simulations (DNS) of isotropic turbulence, observed that heavy particles collect preferentially in regions of low vorticity and high strain rate. Pan and Banerjee [5] numerically investigated the effects of near-neutral density solid particles on a turbulent channel flow. They reported that particles smaller than the dissipative length scale reduce the turbulence intensity and Reynolds stresses, whereas particles that are somewhat larger increase intensity and stresses. Li *et al.* [6] numerically studied the behavior of particle-laden gasses in a small Reynolds number vertical downward channel flow. Effects of particle–particle collisions are considered in their work. They reported that particle feedback forces cause the turbulent structures to become more anisotropic as the particle concentration is increased. For small mass fractions, the particles cause an increase in the gas flow rate. Also, particles tend to increase the characteristic length scale of the fluctuations in the streamwise components of velocity. Most recently, Richter and Sullivan [7, 8] performed a series of DNS to highlight the role of sea sprays in the momentum transfer between the atmosphere and the ocean. Sea spray droplets were modeled as heavy inertial particles suspended in a turbulent airflow, and droplets were represented by solid pointwise particles, whose individual trajectory was tracked over time in a Lagrangian way. They reported that, for typical diameters of sea spray droplets (typically between 10 μm and 1 mm), mechanical effects dominate over the thermal effects. By studying the momentum budget, they introduced a ‘spray’ stress, which compensates for the decrease in Reynolds stresses by providing a feedback effect on the turbulence. They showed that the drag coefficient based on the total stress remains almost unchanged in the presence of sea sprays, while the drag coefficient based on the turbulent stress is reduced. Zhao *et al.* [9] also performed two-way coupled DNS of turbulent channel flows, with a Lagrangian point particle approach. They pointed out that for sufficiently large particle response times (a measure of the particle inertia that will be defined later), the Reynolds shear stresses and the turbulence intensity in the spanwise and wall-normal directions were attenuated, whereas velocity fluctuations were increased in the streamwise direction.

The present work is devoted to the intermediate situation of *two-way coupling* of fluid and particles. Similar to some of the aforementioned recent studies, we perform DNS to study in detail the impact of point particles on properties of turbulent channel flows, in the particle mass fraction range that is relevant to the water (sea) spray particles in a high velocity gas (air) flow. To do so, a three-dimensional (3D) lattice Boltzmann method (LBM) to solve Navier–Stokes (NS) equations is implemented and applied. For the coupling between particles and the fluid carrier phase, a two-way

coupling approach is implemented, in which the particle feedback forces are expressed as distributed volume forces in the LBM. In particular, the effects of particle volume fraction and size are studied on a series of mean and turbulent channel flow properties.

This article is organized as follows: the LBM for solving the fluid flow in the carrier phase is described in Section 2. The Lagrangian particle tracking method is then explained in Section 3. Results for a series of relevant simulations are presented next in Section 4, and conclusions and a discussion of the main results are finally given in Section 5.

2. DIRECT NUMERICAL SIMULATION OF FLUID FLOWS WITH A LATTICE BOLTZMANN METHOD

A 3D model based on an efficient LBM is used in this study for performing DNS of the fluid flow for the carrier phase in particle-laden flows. Such Three Dimensional Direct Numerical Simulation (3D-DNS) on large grids are computationally very demanding and require the use of efficient numerical models and high-performance computing platforms. While essentially solving for similar physics than standard NS solvers, LBMs have several advantages in terms of data locality and parallel computing, and can be very efficiently implemented on CPU clusters and even heavily parallel general purpose graphical processing units (GPGPUs) [10, 11, 14]. Instead of solving the macroscopic NS momentum equations, LBM models solve discretized mesoscopic Boltzmann equations, which are collision–propagation equations, for fluid particles moving on a regular lattice. It can be shown that for sufficiently small values of space and time steps, Mach (**Ma**) and Knudsen (**Kn**) numbers, the LBM solution converges to that of the NS equations.

The Boltzmann equation thus governs particle distribution functions, $f(\vec{x}, t, \vec{\xi})$, which specify the probability of finding a fluid particle at position, \vec{x} at time t , with particle velocity $\vec{\xi}$ [12, 13]. The fundamental Boltzmann equation reads

$$\frac{\partial f(\vec{x}, t, \vec{\xi})}{\partial t} + \vec{\xi} \cdot \frac{\partial f(\vec{x}, t, \vec{\xi})}{\partial \vec{x}} + \vec{B} \cdot \frac{\partial f(\vec{x}, t, \vec{\xi})}{\partial \vec{\xi}} = \Omega, \quad (1)$$

where \vec{B} denotes the external body forces. The left-hand side of the Boltzmann equation is of advection type, while the right-hand side contains the collision operator Ω , which describes the interaction of particles.

2.1. Lattice Boltzmann method governing equations

For flows in a continuum, with a low Knudsen number, discretized velocities \vec{e}_i are introduced to yield a model of reduced computational cost. In this discretized formulation, a particle is only allowed to move from a given grid (lattice) point, in a limited number of directions and for specific distances. With these assumptions, Eq. (1) transforms into a set of discrete Boltzmann equations

$$\frac{\partial f_i(\vec{x}, t)}{\partial t} + \vec{e}_i \cdot \frac{\partial f_i(\vec{x}, t)}{\partial \vec{x}} + \vec{B} \cdot \frac{\partial f_i(\vec{x}, t)}{\partial \vec{e}_i} = \Omega_i. \quad (2)$$

In this work, the 3 dimensions, 19 discrete velocities ($D3Q19$) regular sub-lattice model is used for the discretization of the velocity space around one grid point (Figure 1). The discrete velocities e_i for this model are ($i = 0, \dots, 18$) [14]

$$\vec{e}_i = c \cdot \left\{ \begin{array}{c|cccccccc} 0 & 1 & -1 & 0 & 0 & 0 & 0 & 0 & 0 \\ 0 & 0 & 0 & 1 & -1 & 0 & 0 & 0 & 0 \\ 0 & 0 & 0 & 0 & 0 & 1 & -1 & 0 & 0 \end{array} \right\}, \quad (3)$$

where $c = \Delta x / \Delta t$ is the lattice speed, with Δx the regular lattice space step and Δt the time step. This means that a particle with velocity c will travel one lattice grid cell over one time step.

A finite difference discretization in space and time over a grid cell yields the LBM equation

$$f_i(\vec{x} + \vec{e}_i \Delta t, t + \Delta t) = f_i(\vec{x}, t) + \Delta t \Omega_i + \Delta t F_i, \quad (4)$$

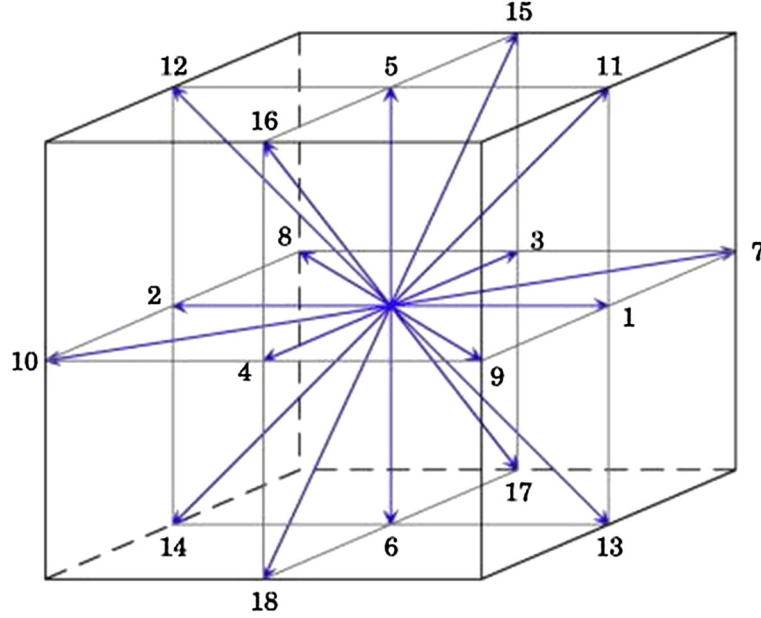


Figure 1. $D3Q19$ sub-lattice model used in the present LBM, where the blue vectors indicate the 18 possible vectors of motion (both direction and length) for a particle to move on the lattice according to Eq. (3.2).

where B_i represents the discretized effects of body forces B_α in Eqs. (22,2). Following Buick and Greated [15], the latter can be expressed as $F_i = w_i \rho_0 e_{ij} B_j / c_s^2$, where $c_s = c / \sqrt{3}$ is the speed of sound, and w_i is the lattice weight factor, which for the $D3Q19$ lattice is

$$w_0 = \frac{1}{3}; w_{1,\dots,6} = \frac{1}{18}; w_{7,\dots,18} = \frac{1}{36}. \quad (5)$$

Equation (4) may be split up into a collision step, during which the particle distribution functions change from equilibrium state due to the collision of the particles, and a propagation step, where the evolved particle distribution functions are moved to the respective neighboring grid points.

$$\bar{f}_i(\vec{x}, t) = f_i(\vec{x}, t) + \Omega_i + \Delta t F_i \quad \text{collision step}, \quad (6)$$

$$f_i(\vec{x} + \vec{e}_i \Delta t, t + \Delta t) = \bar{f}_i(\vec{x}, t) \quad \text{propagation step}. \quad (7)$$

For the collision operator, a so-called multiple relaxation time (MRT) has been used instead of the more widely used single relaxation time collision operator, which is less stable for high Reynolds number flows [13]. In the MRT model, the particle distribution functions are transformed into moment space before relaxation. The moments $m = Mf$ are labeled as

$$m = (\rho, e, \epsilon, j_x, q_x, j_y, q_y, j_z, q_z, 3p_{xx}, 3\pi_{xx}, p_{ww}, \pi_{ww}, p_{xy}, p_{yz}, p_{xz}, m_x, m_y, m_z) \quad (8)$$

and denote the mass density $m_0 = \rho$, the part of the kinetic energy independent of density ($m_1 = e$), the part of kinetic energy square independent of density and kinetic energy ($m_2 = \epsilon$), and the momentum ($m_{3,5,7} = j_{x,y,z}$); $m_{4,6,8} = q_{x,y,z}$ are related to heat fluxes; $m_{9,11,13,14,15}$ are related to the symmetric traceless viscous stress tensor; $m_{16,17,18}$ are third-order moments; and $m_{10,12}$ are two fourth-order moments [16, 17].

The collision operator for MRT reads

$$\Omega_i = \vec{M}^{-1} \vec{S} \left(\vec{M} f - m_i^{eq} \right). \quad (9)$$

M is the transformation matrix from distribution functions to moment space ($m = Mf$ and $f = M^{-1}m$) and is given in [17]; m_i^{eq} are the equilibrium moments given by

$$m_0^{eq} = \rho, \quad m_1^{eq} = e^{eq} = \rho_0 (u_x^2 + u_y^2 + u_z^2), \quad (10)$$

$$m_3^{eq} = j_x^{eq} = \rho_0 u_x, \quad m_5^{eq} = j_y^{eq} = \rho_0 u_y, \quad (11)$$

$$m_7^{eq} = j_z^{eq} = \rho_0 u_z, \quad m_9^{eq} = 3p_{xx}^{eq} = \rho_0 (2u_x^2 - u_y^2 - u_z^2), \quad (12)$$

$$m_{11}^{eq} = p_{zz}^{eq} = \rho_0 (u_y^2 - u_z^2), \quad m_{13}^{eq} = p_{xy}^{eq} = \rho_0 u_x u_y, \quad (13)$$

$$m_{14}^{eq} = p_{yz}^{eq} = \rho_0 u_y u_z, \quad m_{15}^{eq} = p_{xz}^{eq} = \rho_0 u_x u_z, \quad (14)$$

$$m_{2,4,6,8,10,12,16,17,18}^{eq} = 0, \quad (15)$$

where the density has been split up into a constant reference density ρ_0 and a density fluctuation ρ , such that $\rho_{total} = \rho_0 + \rho$. The velocities are derived from the represented momenta: $u_\alpha = j_\alpha / \rho_0$. \bar{S} is a diagonal matrix given by

$$\bar{S} = \text{diag}(0, s_a, s_b, 0, s_c, 0, s_c, 0, s_c, s_d, s_e, s_d, s_e, s_d, s_d, s_d, s_f, s_f, s_f), \quad (16)$$

with $s_d = -\Delta t / \tau$, where τ is a relaxation time computed as a function of the fluid viscosity and the time step as

$$\tau = 3\frac{\nu}{c} + \frac{1}{2}\Delta t. \quad (17)$$

Parameters $s_a, s_b, s_c, s_e, s_d, s_f$ can be chosen freely in the range of $[-2; 0]$. For the $D3Q19$ MRT model, d'Humieres *et al.* [17] use a linear, local analysis to obtain a set of relaxation rates for optimal stability

$$s_a = -1.19, \quad s_b = -1.4, \quad s_c = -1.2, \quad s_e = -1.4, \quad s_f = -1.98. \quad (18)$$

Even though the local analysis does not consider boundary conditions, and therefore, these values are not necessarily the optimal choice for transient, wall-bounded simulations, they were used in all our simulations and considerably improved the stability. Finally, both the velocity and pressure fields are obtained from their respective momenta as

$$u_\alpha = \frac{j_\alpha}{\rho_0}, \quad (19)$$

$$p = \rho c_s^2. \quad (20)$$

It can be shown with Chapman–Enskog expansion that the LBM solution converges to that of the incompressible NS equation

$$\frac{\partial \rho}{\partial t} + \rho \frac{\partial u_j}{\partial x_j} = 0 + \mathcal{O}(\Delta t^2) + \mathcal{O}(\mathbf{Ma}^2), \quad (21)$$

$$\rho \left\{ \frac{\partial u_j}{\partial t} + u_k \frac{\partial u_j}{\partial x_k} \right\} = \frac{\partial \sigma_{jk}}{\partial x_k} + \rho B_j + \mathcal{O}(\Delta t^2) + \mathcal{O}(\mathbf{Ma}^2) + \mathcal{O}(\mathbf{Kn}^2), \quad (22)$$

up to the second order of grid spacing Δx , time step Δt , Mach number \mathbf{Ma} , and Knudsen number \mathbf{Kn} .

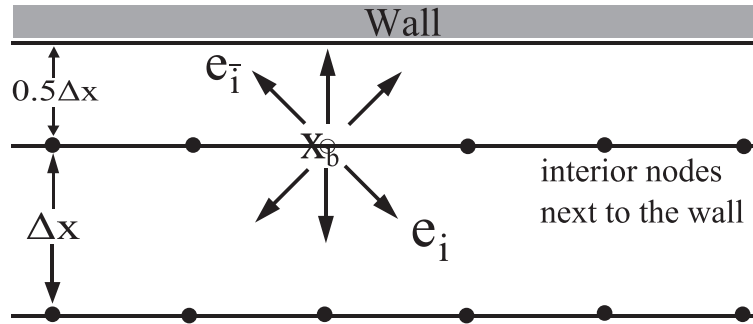


Figure 2. No-slip boundary condition at solid walls: sketch of LBM bounce back on link scheme.

2.2. Boundary condition on solid walls

To simulate no-slip conditions at solid boundaries in the LBM, a so-called ‘bounce back’ boundary condition is specified at the wall, which requires the fluid velocity to be zero at stationary walls. *Bounce back on link* is used in this work, which gives a second order of accuracy in space for straight walls [18] that are placed halfway between two lattice nodes. Note that the flow field calculation is only performed for nodes inside the domain. After the propagation step, the unknown particle distribution functions at the domain boundaries are set equal to the opposite post-collision distribution functions at the same node (Figure 2)

$$f_i(x_b, t + \Delta t) = \bar{f}_{\bar{i}}(x_b, t), \quad (23)$$

the particle distribution functions ‘bounce back’.

3. MODELING OF PARTICLE-LADEN FLOWS

3.1. Key physical concepts

Here, we perform the DNS modeling of turbulent channel flows, for a homogeneous fluid of density ρ_f , kinematic viscosity ν , and velocity u_j (using index notation; $j = 1, 2, 3$), in the presence of a dispersed phase made of a large number of small spherical particles, of density ρ_p and velocity v_j (here, we assume $\rho_p \gg \rho_f$). Such flows were described by Janßen [19], who introduced the following assumptions that will also be made in our study:

- Particles are spherical with diameter d_p and volume $V_p = \pi d_p^3/6$, that is, no shape effects are considered.
- Particles are smaller than the Kolmogorov length scale, that is, $d_p \ll \eta_K$.
- Particles are rigid, that is, no deformation is allowed, and their diameter remains constant.
- The particle Reynolds number is small: $\mathbf{Re}_p = \frac{d_p |u_j - v_j|}{\nu} < 1$, so that Stokes law of drag applies to compute the particle drag force.

Here, because the ratio of densities between the particles (water) and the fluid (air) is large, the particles are referred to as *heavy*. For such cases, the force F_{pj} exerted by the fluid on the particles, and vice versa, will be assumed to result only from the drag contribution, and added mass and lift effects are neglected. In this case, the equation of motion for each particle of mass $m_p = \rho_p V_p$ in the presence of a gravitational acceleration g_j reads

$$m_p \frac{dv_j}{dt} = (\rho_p - \rho_f) V_p g_j + F_{pj}. \quad (24)$$

The time derivative in this equation is a material derivative, following the particle motion. The external force that is applied on each particle consists of three contributions: weight, buoyancy, and drag. The latter is based on the instantaneous relative velocity of the flow at each particle location, and reads

$$F_{pj} = \frac{1}{2} C_D A_p \rho_f (u_j - v_j) |u_j - v_j|, \quad (25)$$

where $A_p = \pi d_p^2/4$ is the particle cross-section and $C_D(\mathbf{Re}_p)$ is the drag coefficient, which is a function of particle Reynolds number \mathbf{Re}_p . Using Stokes law of drag, which is valid for a laminar flow around each particle, we have

$$C_D = \frac{24}{\mathbf{Re}_p}. \quad (26)$$

Combining Eqs. (25) and (26), we find the drag force applied by the fluid on each spherical particle located at x_{pj} ,

$$F_{pj} = 3\pi d_p \nu \rho_f (u_j - v_j), \quad (27)$$

which, by reaction, is also the force applied to the fluid by each particle at the same location.

In the absence of gravity, the drag force exactly balances the particle inertia force, and Eq. (24) yields

$$\frac{dv_j}{dt} = \frac{F_{pj}}{m_p} = a_j, \quad (28)$$

with a_j the particle acceleration.

Combining Eqs. (25) and (28), the particle equation of motion reads

$$\frac{dv_j}{dt} = \frac{(u_j - v_j)}{\tau_p} \quad \text{with} \quad \tau_p = \frac{\rho_p d_p^2}{18\rho_f \nu}, \quad (29)$$

with particle response time τ_p . The particle response time is the key characteristic time scale of the multiphase flows under consideration and physically represents the time that is necessary for the dispersed phase to respond to fluctuations in flow velocity [1]. The larger τ_p , the more inertia the particles have. To the limit, when τ_p is very large, the particle inertia is so large that they behave like ballistic projectiles with their trajectory being nearly unaffected by the fluid flow. By contrast, when τ_p is close to zero, particles act as passive tracers for the flow, because they have so little inertia that they are able to freely follow the fluid motion. In the present context, we will see that the magnitude of τ_p is a crucial factor for determining the behavior of the dispersed phase, by comparing it with a typical time scale of the turbulent flow.

In the following, we further discuss the dimensionless parameters that govern fluid flows with a dispersed point particle phase, that is, the (i) particle Stokes number \mathbf{St} ; (ii) particle volume fraction Φ_{pv} ; (iii) fluid–particle density ratio ρ_f/ρ_p ; and (iv) particle Reynolds number \mathbf{Re}_p . The first two parameters are the two most important ones identified by Elghobashi [1], and the fourth one was already discussed earlier.

(i) Particle Stokes number. This parameter, defined as the ratio of the particle response time to the characteristic time scale of the turbulent flow, qualifies the interactions between the turbulence structures and the dispersed phase. Several different definitions of the Stokes number can be found in the literature, for DNS on wall-bounded turbulence, which usually differ in the selected time scale of the flow. Indeed, the Kolmogorov (turbulent) time scale $\tau_K (\sqrt{\nu/\epsilon})$ and the viscous time scale $\tau_v = \delta_\nu/u_\tau$ can be used to define two different Stokes numbers

$$\mathbf{St}_K = \frac{\tau_p}{\tau_K} \quad \text{and} \quad \mathbf{St}^+ = \frac{\tau_p}{\tau_v} = \frac{\tau_p u_\tau^2}{\nu}. \quad (30)$$

A review of the computational fluid dynamics literature indicates that, in the past 30 years, \mathbf{St}_K has been more widely used to characterize interactions between particle motions and flow structures, mainly because it applies to both isotropic and wall-bounded flows, making it a more universal parameter. However, some recent studies have questioned its relevance for channel flows, in which the dissipation rate is not constant in the wall-normal direction, because ϵ is larger near the walls.

This implies a smaller Kolmogorov time scale near the walls, for a constant fluid viscosity, than at mid-channel width. However, because it is hard to accurately quantify the variation of the dissipation rate across the channel width, most studies have used the time scale calculated at mid-channel width and assumed that it remains unchanged across the channel. By contrast, the viscous time scale does not present this problem as it does not depend on the distance from the wall, because the friction velocity is calculated from the wall stress and fluid density. Hence, for the wall-bounded turbulent flows, it appears more relevant to compare the particle response time with the viscous time scale, rather than with the Kolmogorov time scale. For instance, Richter and Sullivan [7, 8] and Zaho *et al.* [9] used St^+ in their recent studies.

(ii) Particle volume fraction. The volume fraction, Φ_{pv} , quantifies how much of the dispersed phase is present in the flow. It is defined as the ratio of the volume occupied by the particles to the total volume (fluid plus particles)

$$\Phi_{pv} = \frac{N_p \pi d_p^3 / 6}{V_f + N_p \pi d_p^3 / 6}, \quad (31)$$

where N_p denotes the number of particles and V_f the fluid volume. Alternatively, the particle mass fraction can be used to specify the global concentration of particles in the flow. In a similar way to the volume fraction, it is defined as the ratio of the mass of all the dispersed particles $M_p = N_p m_p$ to the total mass of system M_t

$$\Phi_{pm} = \frac{N_p (\rho_p \pi d_p^3 / 6)}{(\rho_f V_f + N_p (\rho_p \pi d_p^3 / 6))} = \frac{N_p D_\rho}{\left(\frac{6V_f}{\pi d_p^3} + N_p D_\rho\right)}, \quad (32)$$

where D_ρ is the density ratio discussed in the succeeding text.

As discussed in Section 1, our work focuses on cases with intermediate volume fractions, $10^{-6} \leq \Phi_{pv} \leq 10^{-3}$, where a two-way coupling assumption between fluid and particle motions is valid. This is the relevant regime to describe interactions occurring between the lower atmospheric turbulence and sea spray droplets at the ocean surface [1]. In this regime, the particle suspension is not so diluted as to prevent particles from affecting flow turbulence or so concentrated that particles would strongly interact with each other (e.g., collisions, coalescence and breakup).

(iii) Density ratio. This is the ratio of the dispersed phase (particles) density over the carrier phase (fluid) density (using Eq. (29))

$$D_\rho = \frac{\rho_p}{\rho_f} = \frac{18\nu}{d_p^2} \tau_p. \quad (33)$$

When considering the forces applied by the carrier fluid onto the dispersed phase, the density ratio helps sort out forces that can be neglected from those that are relevant to the problem (Maxey and Riley [20]). For instance, as seen in Eq.(33), the particle inertia characterized by the particle response time becomes predominant when D_ρ is very large. In our target application, the density ratio is on the order of 1000, which means that particles can be qualified as *heavy*. In applications, the value of D_ρ will remain unchanged unless specified otherwise.

3.2. Numerical algorithm for particle tracking and volume forces

This algorithm solves the particle equation of motion (29) by first-order finite difference (owing to the very small time steps), to compute the velocity v_j of individual particles, as a function of time

$$v_j^{t+\Delta t} = v_j^t + \frac{\Delta t}{\tau_p} (u_j^t - v_j^t) + \mathcal{O}(\Delta t^2). \quad (34)$$

The new position of each particle is then obtained via a second-order Taylor series expansion

$$x_{jp}^{t+\Delta t} = x_{jp}^t + \Delta t v_j^{t+\Delta t} + \frac{1}{2} \Delta t^2 a_j^t + \mathcal{O}(\Delta t^3), \quad (35)$$

where the particle velocity is obtained from Eq. (34) and the acceleration is obtained from Eq. (29).

As this is a Lagrangian time integration following each particle trajectory, the flow velocity u_j must be computed at each particle instantaneous location. In the LBM model, however, velocities are only available at lattice nodes, which require interpolating the velocity field. To do so, we use the accurate and efficient tricubic interpolation scheme of Lekien and Marsden [21]. Once identified, the grid cell in which the particle resides, the method interpolates velocities from neighboring lattice nodes. Because this is a regular lattice, a single set of coefficients (64×64 matrix) is computed and repeatedly used in the interpolations, which save both time and computational resources. In applications, to reduce computational time, particles are released in the fluid flow, once the latter is fully established (i.e., with proper turbulent structures). In this initial stage, particles are uniformly distributed and given the flow velocity at their release location.

The two-way coupling between the fluid and particle phases is operated in the LBM model by way of the volume force term B_j in Eq. (22). For a given lattice cell of volume V_c containing M_p particles, the total volume force per unit mass exerted in the x_j direction is expressed as the opposite of the sum of all the drag forces applied to the particles as

$$B_j = -\frac{1}{\rho V_c} \sum_{p=1}^{M_p} F_{pj}, \quad (36)$$

with F_{pj} the drag force given by Eq. (27) for a single particle. In the LBM model, the contribution B_j to the body force is uniformly distributed to the lattice nodes that are the vertices of the considered cell.

To summarize, in this particle tracking/volume force approach, the following five steps are taken at each time step:

- the tricubic interpolation of the fluid velocity u_j to find its value at the particle positions x_{jp} ;
- the computation of the particle velocities v_j from the fluid velocity field using Eq. (34);
- the time integration to find the new position of each particle using Eq. (35),
- the computation of the forcing terms F_{pj} using Eq. (27) and contribution B_j using Eq. (36), and its distribution to the affected LBM nodes; and
- updating the fluid velocity after taking into account the feedback effect of the particles by solving the complete LBM equations for the fluid phase.

4. RESULTS

The computational domain used in the Three Dimensional Lattice Boltzmann Method (3D-LBM) model for the following DNS of turbulent channel flows is set as follows; no-slip boundary conditions are specified along the lower and upper wall boundaries in the z -direction. These boundaries represent two solid walls separated by a distance $L_z = 2\delta$. Periodic boundary conditions are specified in both the streamwise (x) and spanwise (y) directions, which express that turbulence is homogeneous in these directions.

Next, we specify the grid resolution, in the form of the space step Δx , as a function of the desired Reynolds number. Near the wall, the two important dimensionless parameters are the friction velocity

$$u_\tau = \sqrt{\frac{\tau_w}{\rho_0}}, \quad (37)$$

where τ_w is the wall shear stress, and the viscous length scale

$$\delta_v = \nu \sqrt{\frac{\rho_0}{\tau_w}} = \frac{\nu}{u_\tau}. \quad (38)$$

The friction velocity can be used to define the friction Reynolds number [22]

$$\mathbf{Re}_\tau = \frac{u_\tau \delta}{\nu}, \quad (39)$$

where δ , as defined earlier, is half of the channel width. To compare with earlier seminal work on DNS of single fluid channel flows, we use $\mathbf{Re}_\tau = 180$ in all the applications. Additionally, we found that this value is nearly the lowest possible Reynolds number that can be used to achieve turbulent conditions, which, in return, allow the use of the largest possible domain.

According to Kim *et al.* [23], one of the requirements to achieve turbulent DNS is that the grid resolution has to be fine enough to resolve the smallest turbulent length scales. In particular, the grid spacing should be on the order of the Kolmogorov length scale, which is estimated to be twice the viscous length scale, $\eta_K \simeq 2\delta_\nu$; one also defines $\eta_K^+ = \eta_K/\delta_\nu \simeq 2$ (the superscript + denotes the quantity that is normalized by the viscous length scale). In turbulent channel flows, the grid resolution should be at least equal to the normalized Kolmogorov length scale in the wall-normal direction. We therefore impose the normalized grid resolution to be $\Delta z^+ = \eta_K^+ = 2$ in our configuration. The grid resolution in the other directions does not necessarily need to be as small as the Kolmogorov length scale. However, LBM models normally use regular lattices, where time, space, and velocities are uniformly discretized in all directions, that is, $\Delta x^+ = \Delta y^+ = \Delta z^+$. As a result, in the present case, the flow is over-resolved in the horizontal directions while being appropriately resolved in the wall-normal direction [24]. This situation can be improved upon by using a varying grid resolution in different directions, as will be attempted in future work.

It should be pointed out that in the LBM, the length, time, and mass scales are usually defined in non-dimensional lattice units. Here, the symbols L , T , and M are defined to characterize the length, time, and mass scales, respectively, used in the lattice units. In particular, the grid spacing $\Delta x = 1L$ is set to unity in lattice length scale and time step $\Delta t = 1T$ to unity in lattice time scale. Thus, lattice speed $c = \Delta x/\Delta t$ is equal to $1 L/T$ in lattice unit. As discussed previously, the LBM is based on a weakly compressible formulation that converges to the incompressible NS equations in the limit of small Mach numbers \mathbf{Ma} . Hence, even though dealing with essentially incompressible flows, the Mach number must be specified as a parameter. The Mach number of the present simulations is based on the mean centerline velocity in the channel flow, which is the maximum mean velocity in the simulation.

The speed of sound is $c_s = c/\sqrt{3} = 0.577L/T$ in lattice unit. Hence, to yield a low mean Mach number $\mathbf{Ma} = 0.2$, the mean centerline velocity was set to $U_0 = 0.115L/T$ in lattice unit. The theoretical velocity profile for a wall boundary layer can be expressed by the log law [22]

$$U_0^+ = \frac{1}{\kappa} \ln(\mathbf{Re}_\tau) + A, \quad (40)$$

with $A = 5.5$ and $\kappa = 0.4$, which can be used to express the relationship between centerline velocity U_0 and friction velocity u_τ , $U_0^+ = U_0/u_\tau$.

In the applications, given the Mach and friction Reynolds number values, we obtain the mean velocity U_0 , and Eq. (40) can be used to calculate the friction velocity. For $\mathbf{Ma} = 0.2$ and $\mathbf{Re}_\tau = 180$, the friction velocity obtained from this equation is $u_\tau = 0.00622L/T$ in lattice unit. With $\Delta x = 1L$, and the minimum requirement $\Delta x^+ = 2$, the viscous length scale is set to $\delta_\nu = 0.5L$. Then, the kinematic viscosity of the simulation is computed from the definition of the viscous length scale (Eq. 38); here, we find, $\nu = 0.00311L^2/T$, which based on Eq. (17) yields the relaxation time in LBM simulations, $\tau = 0.5093T$.

Based on the definition of the friction Reynolds number in Eq. (39), we find the half width between walls to be $\delta = 90L$, and, hence, the total number of lattice nodes in the wall-normal direction z to be $2\delta/\Delta x = 180$ (Figure 3). Note, from the implementation of the bounce back on link boundary condition, that the first nodes next to the wall are placed at $0.5\Delta x$ ($\Delta x^+ = 1$) away from the wall. Because of the restriction of the numerical implementation to use single GPG-PU only (with a maximum device memory of 6 GB), the maximum lattice grid size that could be achieved was, $260 \times 260 \times 180$ (12.2 million nodes), in the x -direction, y -direction, and z -direction, respectively, which corresponds to a domain size of $(2.9\delta, 2.9\delta, 2\delta)$.

Thus, to investigate the convergence of flow fields toward KMM's results, we ran three DNS for a single fluid, using varying grid sizes, while maintaining the distance between walls to 2δ as in KMM. Besides case A, we also modeled a larger channel in case B, with dimensions of $3.9\delta \times 3.4\delta \times 2\delta$ ($350 \times 300 \times 180$ lattice nodes; 18.9 million), which is about the largest size achievable on one GPGPU without particles, and finally the largest grid in case C, with $6.7\delta \times 3.4\delta \times 2\delta$ ($600 \times 300 \times 180$ lattice nodes; 32.4 million), for which we used two GPGPUs. Note that this single attempt at using

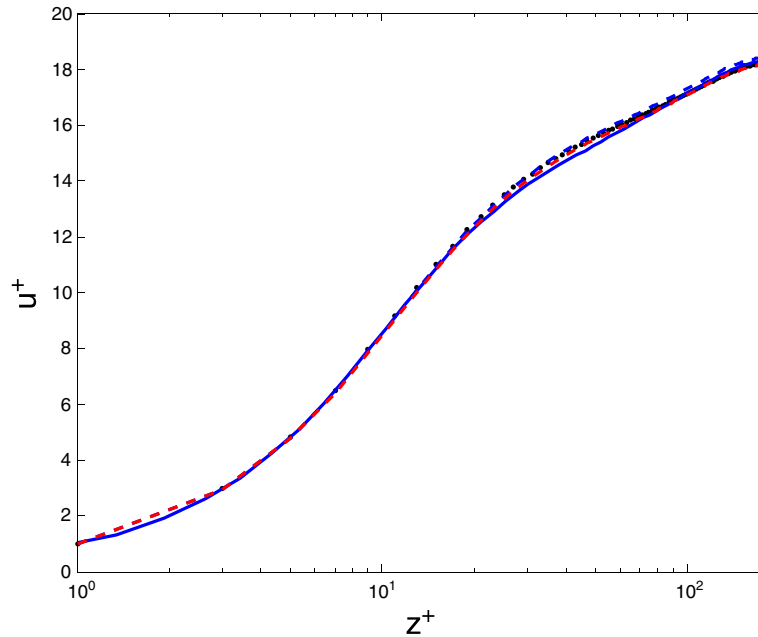


Figure 4. Validation of turbulent channel flow simulations. Mean streamwise velocity: KMM (blue solid line), case A (black dotted line), case B (blue dashed line), case C (red dashed line).

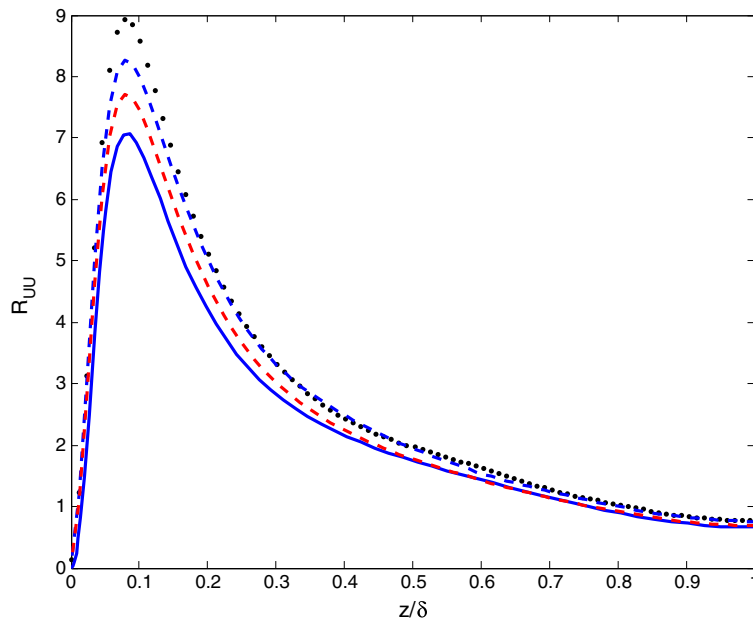


Figure 5. Validation of turbulent channel flow simulations. Reynolds shear stress $-\overline{u'u'}$, normalized by the wall shear velocity: case A (black dotted line), case B (blue dashed line), case C (red dashed line), and KMM (right panel).

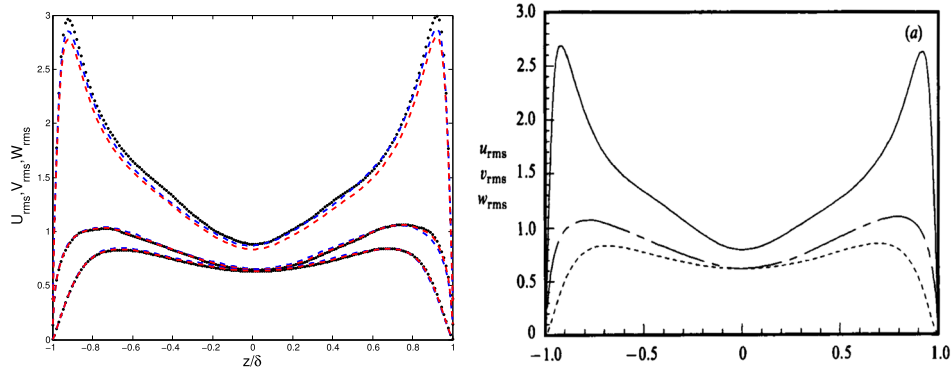


Figure 6. Validation of turbulent channel flow simulations. Root mean square velocity fluctuations normalized by the wall shear stress: KMM (blue solid line), case A (black dotted line), case B (blue dashed line), and case C (red dashed line).

two GPGPUs is only applicable to single fluid flows, and this model has not yet been extended to particle-laden flows, for which the management of particles moving between GPGPU regions and flow interpolation is much more complicated.

Figures 4, 5, and 6 show the mean streamwise velocity, normalized Reynolds stresses, and root mean square velocities computed for cases A, B, and C, respectively, in comparison with KMM's results. While differences for the mean streamwise velocity are quite small for all cases, for the turbulent properties, as should be expected, LBM results obtained in the larger domains B and C are in better agreement with KMM's benchmark study, with case C results having nearly converged to those of KMM. Even for case A, however, results are in reasonable agreement with KMM's results, which allows using this case for studying effects of the dispersed particle phase on turbulent flow properties. Clearly, however, more accurate results would be obtained for larger grids, which require using several GPGPUs for the particle-laden flow simulations as well. This will be left out for future work.

4.2. Turbulent particle-laden flow simulations

As explained earlier, the turbulent particle-laden flow simulations are performed on the grid A. Four non-dimensional parameters have been previously identified that govern the dynamics of turbulent particle-laden flows. In the present simulations, the flow Reynolds number and particle density ratio are kept constant while varying the concentration (mass fraction) and size (Stokes number) of the particles. Table I summarizes the different cases that were simulated. Numerical results for each case are presented and discussed in the following sections. Figures will be presented as a series of curves corresponding to the various cases, obtained first by varying the mass fraction (at constant Stokes number) and then by varying the Stokes number (keeping the mass fraction constant). Line codes in figure legends are kept identical throughout and are listed in Table II.

4.3. Mean and root mean square (RMS) flow velocity

The effects of particles on the turbulence can be observed in the mean streamwise velocity of the carrier fluid across the channel width, shown in Figure 7 in semi-log scale and in Figure 8 in linear scale. In the presence of particles, the mean flow velocity decreases in the logarithmic region and near the center of the channel relatively to the clean channel case while it is nearly unchanged near the walls.

More specifically, for particle-laden flows, the mean velocity profiles are all found to be below the baseline profile from $z^+ \approx 20$ (i.e., beyond the viscous wall region) to the center of the channel, while they remain very close to the clean channel profile near the wall. In the case where the mass fraction increases from 0.1 to 0.25 and then to 0.5 (left panels), a consistent decrease of the velocity can be noted, with the largest difference occurring for case IV. The right panels indicate that the

Table I. Turbulent particle-laden flow simulations. Particle properties for seven different DNS, using $\mathbf{Re} = 180$ and $D_\rho = 1000$. The particle diameter d_p^+ has been normalized using the viscous length scale.

Case	N_p	Φ_{pm}	\mathbf{St}^+	d_p (μm)	d_p^+
Clean channel	0	—	—	—	—
I	6×10^5	0.25	10	26	0.104
II	4.6×10^4	0.10	30	45	0.18
III	1.2×10^5	0.25	30	45	0.18
IV	2.3×10^5	0.5	30	45	0.18
V	2.3×10^4	0.25	90	78	0.312
VI	985	0.25	720	220	0.88
VII	1980	0.5	720	220	0.88

DNS, direct numerical simulations.

Table II. Line codes in figure legends for simulation cases listed in Table I.

DNS runs	Case	Color, symbol
Baseline	Clean channel	Black solid line
Effects of concentration	II	Blue dotted line
	III	Blue solid line
	IV	Blue dashed line
Effects of particle size	I	Blue dotted line
	III	Blue solid line
	V	Blue dashed line
Effects of large particles	VI	Red solid line
	VII	Red dashed line

DNS, direct numerical simulations.

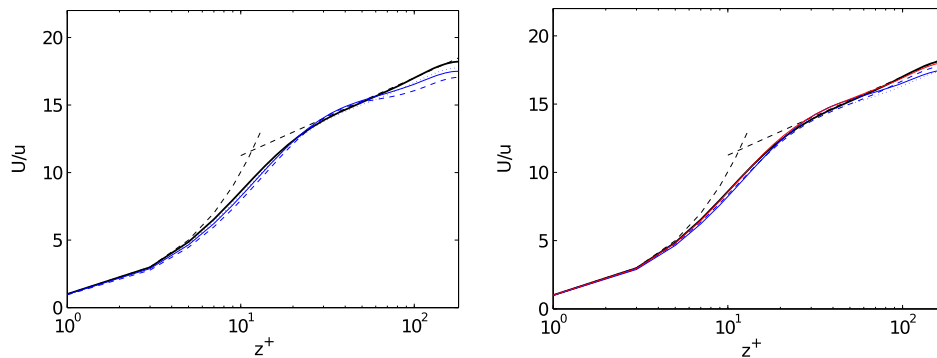


Figure 7. Turbulent particle-laden flow simulations. Mean streamwise velocity (log scale), normalized by the friction velocity. Left: as a function of increasing mass fraction: cases II, III, and IV ($\mathbf{St}^+ = 30$). Right: as a function of increasing Stokes number: cases I, III, IV, and VI ($\Phi_m = 0.25$).

discrepancy with the baseline (clean channel) is largest for case I (i.e., the smallest particles) and is *reduced* for the larger particles. The impact nearly disappears for case VI ($\mathbf{St}^+ = 720$, $\Phi_{pm} = 0.25$). This suggests that the smaller particles (for the particle size range investigated) are more effective in modifying the mean profile, given a constant mass fraction. Among all the cases, case IV ($\mathbf{St}^+ = 30$, $\Phi_m = 0.5$) shows the highest impact on $\langle u \rangle$.

Next, Figure 9 shows the root mean square of turbulent velocity fluctuation components computed across the channel. This is the primary statistics of turbulence, where effects of particles can be easily observed. In general, the presence of particles increases the streamwise turbulence intensities while reducing the spanwise and the wall-normal components. For increasing particle concentration, the streamwise fluctuations are larger relative to the baseline of the clean channel. The increase is

TURBULENT PARTICLE-LADEN CHANNEL FLOW

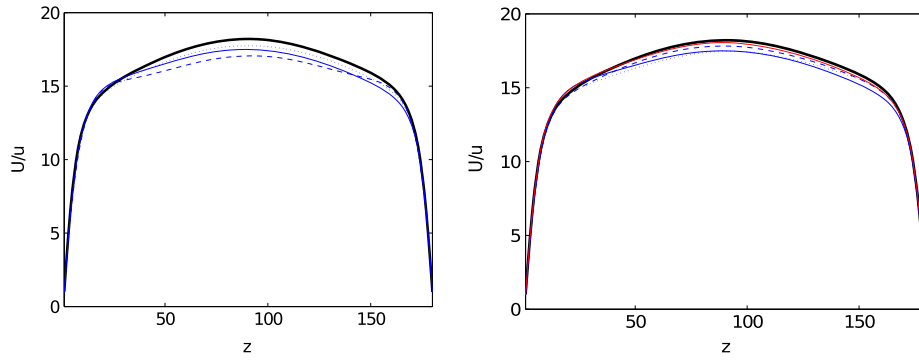


Figure 8. Turbulent particle-laden flow simulations. Same results as in Figure 7 in linear scale.

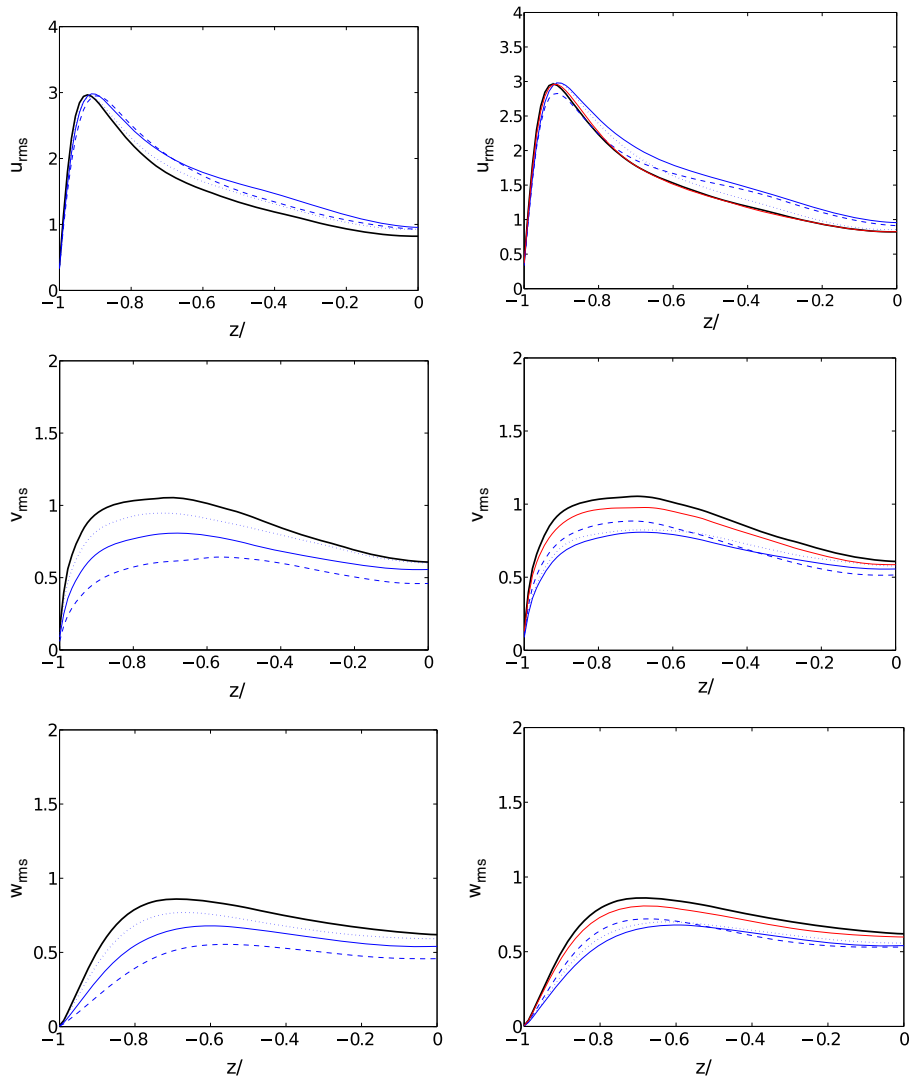


Figure 9. Turbulent particle-laden flow simulations. Root mean square velocity fluctuations. Top: stream-wise, middle: spanwise, bottom: wall-normal. Left: increasing mass fraction, right: increasing Stokes number. See Figure 7 for details of cases.

non-monotonic, however, and happens mainly outside the viscous sublayer, after the maximum of the fluctuations has been reached (around $z/\delta \approx -0.9$). The spanwise and wall-normal fluctuations noticeably drop across the channel width, as compared with the baseline, and the maximum of each curve is displaced further away from the wall. The disparity with the clean channel becomes more pronounced when a larger number of particles are dispersed in the flow. For increasing Stokes number, the streamwise velocity fluctuations are higher than for the clean channel, although the difference is negligible for case VI. The enhancement of the streamwise fluctuations is particularly evident for cases III and V. Dampening of the y -fluctuation and z -fluctuation components can be seen in all cases. Moreover, case I with the smallest particles displays an interesting behavior: the curves for v_{rms} and w_{rms} start at the wall between cases III and V, but end up crossing the curves beyond the viscous wall region.

Overall, we may conclude that there is a global effect of Φ_{pm} and St^+ on the lower-order statistics of turbulence, although the underlying mechanisms of turbulence modulation may be different whether St^+ or Φ_{pm} is changed in the DNS runs. According to Zhao *et al.* [9], it is thought that the inertia of particles may play an important role in modifying the low-order moments of turbulence, at any concentration. The attenuation of the wall-normal fluctuations, combined with the enhancement of the streamwise turbulence intensities, has a profound impact on many aspects of turbulent channel flows.

4.4. Streamwise force balance

One way to verify that the two-way coupling approach is correctly implemented in the LBM model is to compute a streamwise force balance between the feedback volume force, which is included in the LBM equation, as a result of momentum exchanged between the fluid and the dispersed phase and other components of the momentum balance, in the streamwise x -direction. Once we verify that the conservation of momentum is satisfied, we can focus on understanding the particles' role in the global force balance. The 'mean' operator (denoted by the angle brackets) here refers to results that are both spatially averaged in the streamwise and horizontal plane directions and time averaging over the simulation after the statistically steady state has been reached.

In the case of the clean channel, the force balance consists of the mean viscous force and the Reynolds force, which should be exactly compensating the mean pressure gradient

$$F_V + F_R = \frac{\partial \langle p \rangle}{\partial x}, \text{ with } F_V = \frac{\partial}{\partial z} \left(\mu \frac{\partial \langle u \rangle}{\partial z} \right) \text{ and } F_R = -\frac{\partial}{\partial z} (\rho_f \langle u' w' \rangle). \quad (42)$$

Note that while many studies examine the stress balance and compute the viscous and Reynolds stresses in turbulent Poiseuille DNS, examining the force balance is more relevant in the case where particles are dispersed in the computational domain. We emphasize that both formulations are equivalent, and we can relate the forces described in Eq. (42) to the viscous and Reynolds stresses as

$$\tau_V = \mu \frac{\partial \langle u \rangle}{\partial z} \text{ and } \tau_R = -\rho_f \langle u' w' \rangle.$$

In the case of particle-laden flows, the force balance becomes

$$F_V + F_R + F_p = \frac{\partial \langle p \rangle}{\partial x}, \text{ with } F_p = \rho_f \langle B_1 \rangle, \quad (43)$$

where B_1 denotes the x -component of the particle feedback volume force computed with Eq. (36).

Figure 10 shows the repartition of the various forces for channel flow simulations, as a function of the normalized distance from the wall. [Note that the legend in this figure differs from that of the previous plots.] The first plot corresponds to the clean channel case, where we see that the sum of the viscous and Reynolds forces nearly exactly compensate the mean pressure gradient applied to the flow (within a small numerical error). This shows that there is no sink or source of momentum in the channel flow DNS, confirming the accuracy of the LBM solution. The second plot illustrates the repartition of the forces among viscous, Reynolds, and particle feedback forces, for cases II, III, and IV (for increasing particle concentration), while the third plot shows a similar family of curves,

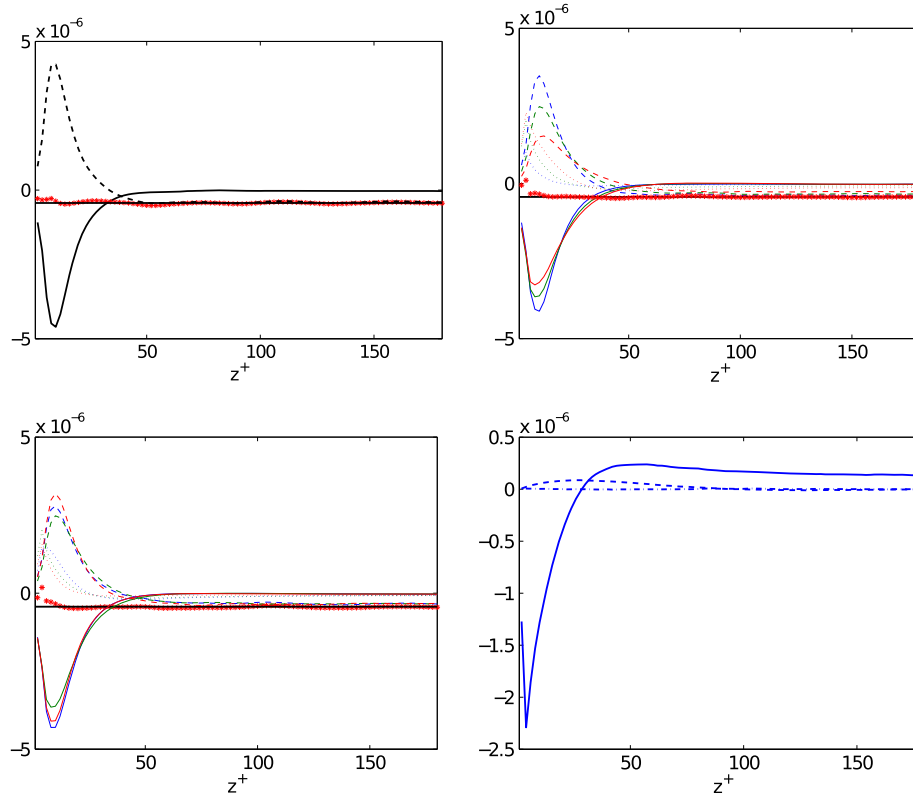


Figure 10. Turbulent particle-laden flow simulations. Average force balance in streamwise direction: clean channel (upper left); varying mass fraction (upper right: case II—blue, III—green, and IV—red); varying Stokes number (lower left: case I—blue, III—green, and V—red); and particle force components for case IV (lower right). Legend for the first three plots: viscous force F_V (solid line), Reynolds force F_R (dashed line), particle feedback force F_p (dotted line), pressure gradient $\partial\langle p \rangle / \partial x$ (black thin horizontal line marked at $-4.34 \times 10^{-7} ML^{-2} T^{-2}$), and sum of all forces (red starred line). Legend for the last plot: $\langle B_1 \rangle$ (solid line), $\langle B_2 \rangle$ (dashed line), $\langle B_3 \rangle$ (dashed dotted line).

for cases I, III, and V (for increasing Stokes number). The last plot, on the lower right, shows the force components, for the case with the largest concentration of particles (case IV).

As expected, for the clean channel case, the absolute value of the viscous force is maximal in the viscous layer [22], and reaches zero beyond the buffer layer ($z^+ \approx 30$). The Reynolds force has an opposite sign to the viscous force, and balances it by reaching the value of the mean pressure gradient at the point where viscous effects vanish away from the wall. The effect of an increasing particle mass fraction on the force balance can be seen in the second plot, in the upper right corner: inside the viscous sublayer, the magnitude of both the viscous force and the Reynolds force progressively decreases, while the particle force $\langle B_1 \rangle$ increases at the same time. A small discrepancy between the sum of the forces and the mean pressure gradient is observed near the wall, which is likely due to the treatment of the no-slip boundary condition in the LBM (bounce back scheme). Similar observations can be made in the third plot (lower left) for the forces and force balance for the case of an increasing Stokes number. Again, the magnitude of the forces is smaller than for the clean channel case. However, the evolution of the forces is non-monotonic: the curves for case I are found between cases III and V (Reynolds force) and case V (viscous force). The lesser impact of particles is seen for case VI (not plotted here), which is expected because it corresponds to the smallest amount of particles. In both cases (second and third plots), besides the numerical artifact near the wall, it is clear that the force balance is well-satisfied across the channel width in the presence of dispersed particles, thus confirming the relevance and accuracy of the proposed Lattice Boltzmann Method-Direct Numerical Simulation (LBM-DNS) approach for two-way coupled particle–fluid problems.

Additional observations are that the Reynolds force decreases faster than the viscous force near the wall for increasing mass fraction or Stokes number. On the other hand, for cases II, III, and IV, the locations of the particle force maxima are closer to the wall than the maxima of both F_V and F_R , which indicate that the particles impact the turbulence mainly close to the wall, rather than in a homogeneous fashion over the whole domain. While the particle force magnitude can reach up to five times that of the mean pressure gradient, it remains very localized in the domain. Outside the viscous sublayer, the particle force is small but remains finite, and reduces the Reynolds force accordingly. Lastly, the fourth plot in Figure 10 on the lower right shows the mean particle force component variation across the channel for case IV. As expected, $\langle B_1 \rangle$ in the streamwise direction provides the maximum contribution, while $\langle B_3 \rangle$ is zero everywhere. It is interesting to note that $\langle B_2 \rangle$ is not zero near the wall, but its magnitude is much smaller than that of $\langle B_1 \rangle$.

From Figure 10, we may conclude that regardless of their size or concentration, small inertial particles allowed to interact directly with the carrier fluid impact the distribution of the forces by dampening the Reynolds force (across the channel) and the viscous force (within the viscous wall region).

4.5. Production and dissipation of mean turbulent kinetic energy

Zhao *et al.* [9] investigated particle effects on the mean TKE budget of particle-laden fluid flows, focusing on the energy transfer between the fluid and the particle phases and on the dissipation rate in the wall turbulence. This budget is based on a conservation equation that can be derived from the NS Eqs. (21) and (22) as

$$\begin{aligned} \frac{Dk}{Dt} = & -\frac{1}{\rho_f} \frac{\partial \langle u'_i p \rangle}{\partial x_i} - \frac{\partial \langle k u'_i \rangle}{\partial x_i} + \nu \frac{\partial^2 k}{\partial x_j \partial x_j} \\ & - \langle u'_i u'_j \rangle \frac{\partial \langle u_i \rangle}{\partial x_j} - \nu \frac{\partial \langle u'_i u'_j \rangle}{\partial x_j \partial x_j} + \langle u'_i B'_i \rangle, \end{aligned} \quad (44)$$

with $k = (1/2)\langle u'_i u'_i \rangle$ the mean TKE, in which there are seven terms, from left to right, of the mean TKE: (i) time rate of change; (ii) pressure transport; (iii) turbulent transport; (iv) viscous diffusion; (v) production; (vi) dissipation rate; and (vii) particle production.

For a statistically stationary turbulent channel flow, the mean TKE is conserved, and its time rate of change, which is expressed in the left-hand side of Eq. (44) by a material derivative, corresponding to the sum of a local rate of change and the advection of k by the mean flow, must be equal to zero. Because gravity has been neglected in this work, buoyancy does not intervene in the mean TKE balance. Here, we are mainly interested in the repartition of mean TKE among production terms and the dissipation rate. We will denote the mean TKE production by P (mean-shear production), particle production by P_p , and dissipation rate by ε . In wall-bounded turbulent flows, the production term P can be simplified to

$$P = \langle u'w' \rangle \frac{\partial \langle u \rangle}{\partial z}.$$

Figure 11 plots P , P_p , and ε across the channel width, for cases I to VI, with the clean channel results being shown as a baseline. The left side figures represent cases II, III, and IV with increasing mass fraction; because of particle feedback effects, we see a reduction of the TKE mean production and the presence of a non-zero production term P_p . The magnitude of the dissipation rate also decreases with increasing mass fraction. The top and bottom panels show that the particle production is small compared with the TKE production, and negative across the channel width for cases III and IV. The fact that P_p becomes negligible for case II is due to the very low concentration of particles dispersed in the flow. The right side figures represent cases with increasing Stokes number; we see that particles of various diameters impact in a different and complex manner the TKE production and dissipation terms, although both the production and dissipation terms are reduced in the presence of particles. The impact is much smaller however for case VI ($\text{St}^+ = 720$, $\Phi_{pm} = 0.25$), which has a very small number of particles. We also see that the particle production term changes sign for some

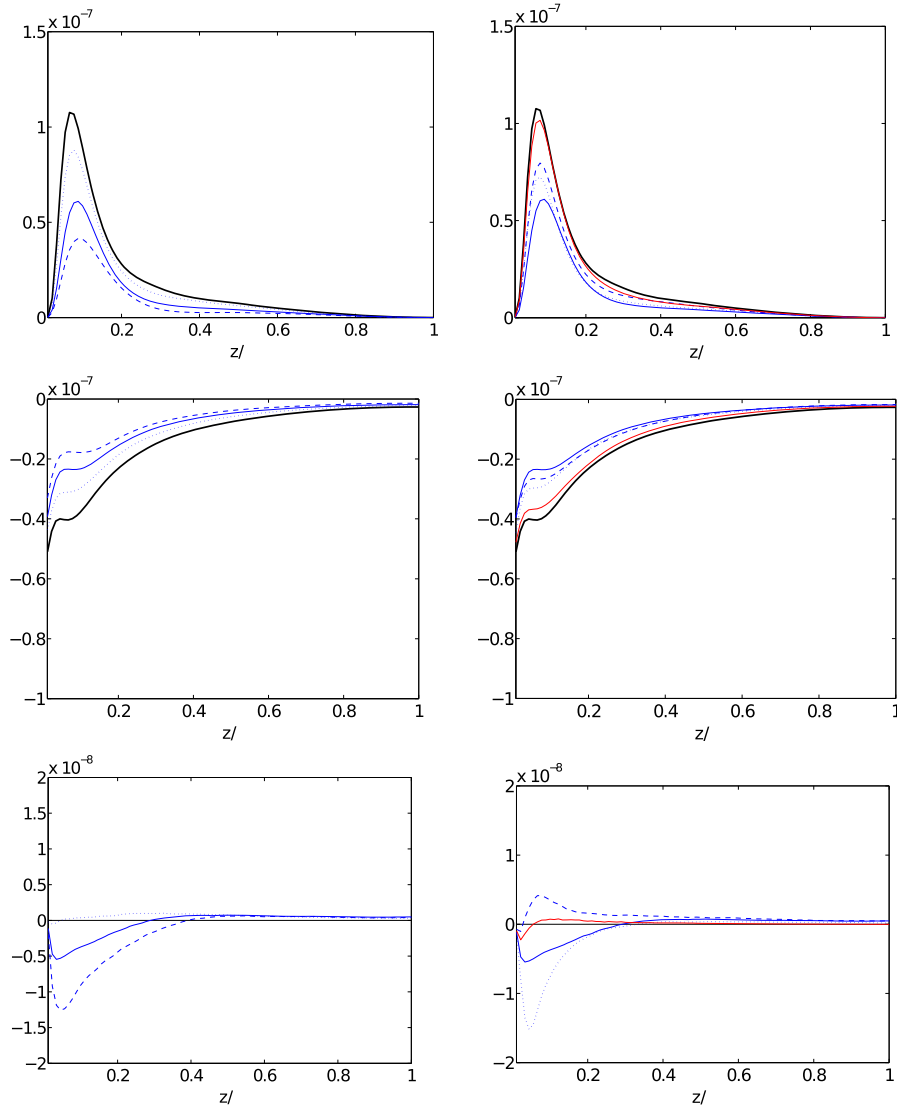


Figure 11. Turbulent particle-laden flow simulations. TKE production and dissipation terms, across the channel width. Top: P , middle: ε , bottom: P_p . Left: cases with increasing mass fraction. Right: cases increasing Stokes number. See definitions in Table II.

cases, being mostly negative for cases I and III, then positive across the channel width for case V, and finally nearly zero for case VI, where, as indicated, very few particles were dispersed in the flow (like in case II).

To summarize, the introduction of many small particles in a turbulent channel flow modifies the TKE budget across the channel width, in the wall-normal direction, although change is not monotonic and varies depending on values of the mass fraction and Stokes parameters. The fine turbulent flow structures that influence the TKE production and dissipation are further discussed in the next section.

4.6. Turbulent coherent structures

It is commonly accepted in the wall turbulence research community that turbulence appears in the flow as organized structures, spanning several length and time scales [25]. According to Adrian [26], wall turbulence is characterized by the presence of packets of hairpin vortices and associated quasi-streamwise vortices (QSVs) near the walls. Such turbulent structures, which are referred to

as *coherent* because they persist for a long time in the flow, have been extensively studied both experimentally and numerically. In particular, a mechanism for generating QSVs in a turbulent channel flows was suggested by Zhou *et al.* [27]. They argued that the turbulent boundary layer contains a large number of hairpin vortices, aligned in the streamwise direction as coherent packets. Although they first studied the evolution of a single idealized symmetric hairpin vortex, they also investigated asymmetric hairpin vortices and concluded that QSVs generated from asymmetric structures occurred more often singly and rarely as counter-rotating pairs of equal strength. Zhou *et al.* added that asymmetric vortex generation was more frequently observed experimentally in turbulent boundary layers. Moser *et al.* [28] investigated the role of near-wall coherent structures in turbulent channel flows and proposed a model with overlapping and alternating sign QSVs, as the dominant near-wall coherent structures (Figure 12). Note, similar to KMM’s study, that the convention used in this figure for the coordinates is that the y -direction corresponds to the wall-normal direction.

Figure 13 shows the instantaneous snapshots of streamwise velocity u from a side view (x - z), as well as the second component of vorticity ω_y (rotation around our y -direction). Vorticity is computed by a finite difference scheme, based on its general definition

$$\omega_i = \epsilon_{ijk} \frac{\partial u_k}{\partial x_j},$$

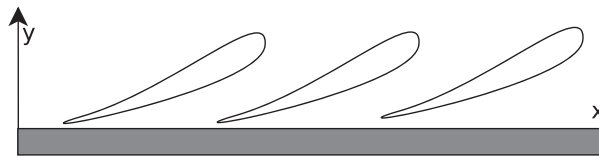


Figure 12. Schematics of an array of quasi-streamwise vortices (QSV).

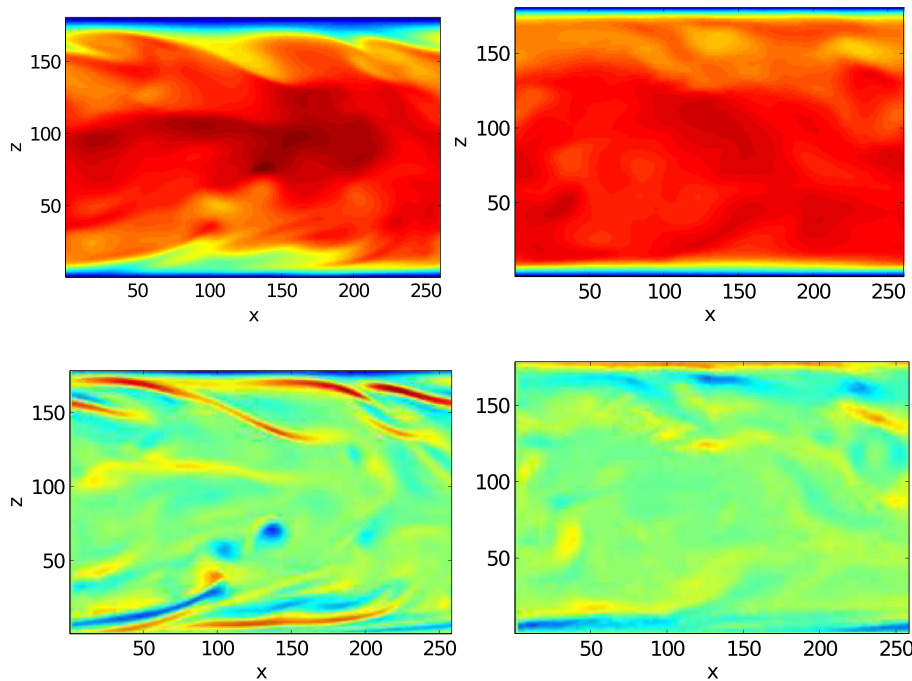


Figure 13. Turbulent particle-laden flow simulations. Instantaneous snapshots of (upper left) streamwise velocity u for the clean channel, (upper right) streamwise velocity for case IV, (bottom left): vorticity ω_y (rotation around y -direction) for the clean channel, and (bottom right) vorticity for case IV.

with ϵ_{ijk} being the third-order antisymmetric unit tensor. For channel flow turbulence, where the flow is strongly anisotropic, the vorticity component of interest is

$$\omega_y = \frac{\partial u}{\partial z} - \frac{\partial w}{\partial x},$$

which can be computed based on LBM results at various lattice nodes at a given time as

$$\omega_y = \frac{1}{10\Delta x} (2w_{i+2,j,k} + w_{i+1,j,k} - w_{i-1,j,k} - 2w_{i-2,j,k}) - \frac{1}{10\Delta z} (2u_{i,j+2,k} + u_{i,j+1,k} - u_{i,j-1,k} - 2u_{i,j-2,k}).$$

Snapshots in Figure 13 clearly capture the dominant turbulent structures in the computational domain. In particular, for the clean channel flow, the pattern of vorticity seen in the lower left corner figure matches the locations of the slower streamwise velocity in the upper left corner plot. Comparing these simulations to the schematics of Jeong *et al.* [29] in Figure 12 suggests that the structures of positive and negative vorticities Ω_y indeed correspond to QSVs, or more generally to turbulent coherent structures. In the upper left corner plot, the enforced no-slip boundary condition results in a thin blue layer near each wall, where the streamwise velocity $u \approx 0$. Conversely, the velocity is maximum near the center of the channel. The upper right plot shows, for particle-laden flows, the striking absence of the coherent structures near the walls, as well as a reduction of the velocity at the centerline of the channel. Vorticity in the lower right plot is also significantly reduced, except for a few traces of negative vorticity near the walls. It is evident that the major effects of small

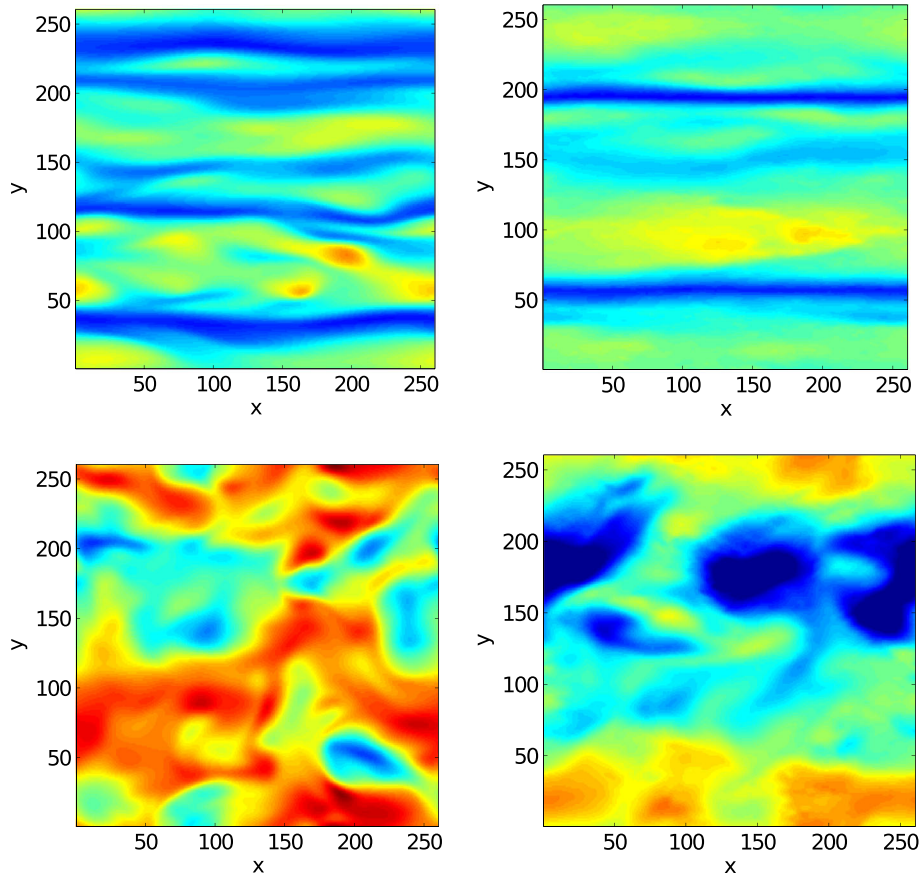


Figure 14. Turbulent particle-laden flow simulations. Snapshots of velocity fluctuations in horizontal (x - y) planes. Clean channel flow (left plots), case IV (right plots).

inertial particles in the flow are to dampen the turbulent coherent structures near the boundaries of the channel.

Patterns observed for the streamwise velocity and QSVs are further investigated in Figure 14, where the left side plots are for the clean channel, and the right side plots are case IV particle-laden flow. The upper plots show the streamwise velocity u observed from a top view (x - y plane) at a small distance from the channel bottom wall, while the lower plots show the u at the mid-channel width. The scale of velocity at the channel center (from 0.1 to 0.12) takes into account the fact that the velocity at the center of the channel has a large mean value and smaller fluctuations. Consistent with Figure 13, in the upper plots, we see that turbulent structures near the wall are drastically modified by the particles. The vortices present in the clean channel flow are weakened under the action of particles, leading to less low-speed regions near the wall. In the lower plots, the effects of particles on turbulent structures are less obvious, other than the fact that the mean velocity is slightly reduced.

5. CONCLUSIONS

In this work, we efficiently implemented, on a heavily parallel GPGPU board, a 3D-LBM model for DNS of turbulent particle-laden flows and used it to simulate and study a variety of channel flow turbulent properties, as a function of various mass fractions, numbers, and sizes of particles.

We first validated the fluid only model by simulating turbulent boundary layer flows, in a periodic channel with two solid walls without particles, and comparing the results with those of the reference paper by Kim *et al.* [23]. We concluded that, despite using a smaller computational domain in the wall-parallel directions than normally necessary to resolve all the turbulent eddies, our results were in good agreement with KMM's results, in particular for statistics of turbulent fields (e.g., mean velocity and normalized Reynolds stresses). In the absence of particles, larger computational domains were used on a single GPGPU and even larger using two GPGPUs, which showed a clear convergence of LBM toward KMM's results. In the presence of particles, the LBM grid has to be smaller on the single GPGPU, and clearly, this is a limitation of the present simulations. Future work could extend the simulation of particle-laden flows to multiple GPGPUs. Nevertheless, this validation study confirmed that turbulent flow properties were adequately simulated in the selected model grid, particularly in the vertical direction, to allow accurately studying particle effects on turbulent properties and structures.

Hence, next, we explored the effects of having a dispersed phase made of many small inertial particles in turbulent channel flows. Once particles were properly dispersed in the flow, we performed several DNS runs by varying the particle concentration and size (i.e., the mass fraction: Φ_m and the viscous Stokes number St^+). Overall, compared with the clean channel, these DNS showed that effects of particles are to reduce the mean streamwise velocity, turbulent structures, and intensity near the walls, and spanwise and wall-normal velocity fluctuations, while accentuating streamwise turbulent intensities and velocity fluctuations.

The momentum conservation and force balance were computed as well. In the clean channel case, the Reynolds and viscous forces compensate each other, so that their sum is equal to the mean pressure gradient applied to sustain the mean flow. With particles (cases I–VI), feedback force appears in the force balance, and a new force distribution takes place: both the Reynolds and viscous forces are much lower than in the clean channel case, while the particle force progressively increases for larger mass fractions and decreases for larger Stokes number (because a lower number of particles is required to reach the given mass fraction of 0.25 for cases V and VI). Additionally, the TKE budget, including the mean-shear production (P), dissipation rate (ϵ), and particle production (P_p) were evaluated. The particle production is usually small relative to the flow production term, and can change sign depending on the particle size (cases I and III: $P_p < 0$, case V: $P_p > 0$, and case VI: $P_p \approx 0$). Both P and ϵ are found smaller than for the clean channel case, in all six cases studied with particles, implying that the general effect of particles on turbulence is to reduce its production and attenuate the dissipation. Finally, we investigated the interactions between the

turbulent coherent structures and the dispersed phase. From the various snapshots of instantaneous velocity and vorticity, we may argue that the coherent structures (QSV and sweeps) are weakened near the channel walls in the presence of particles.

ACKNOWLEDGEMENT

The authors wish to acknowledge support from grant OCE-09-27014 of the US National Sciences Foundation (NSF) Physical Oceanography Program.”

REFERENCES

1. Elghobashi S. On predicting particle-laden turbulent flows. *Applied Scientific Research* 1994; **52**:309–329.
2. Balachandar S, Eaton JK. Turbulent dispersed multiphase flow. *Annual Review of Fluid Mechanics* 2010; **42**: 111–133.
3. Rashidi M, Hetsroni G, Banerjee S. Particle turbulence interaction in a boundary layer. *International Journal of Multiphase Flow* 1990; **16**:935–949.
4. Squires KD, Eaton JK. Particle response turbulence modification in isotropic turbulence. *Physics of Fluids* 1990; **A2**:1191–1203.
5. Pan Y, Banerjee S. Numerical simulation of particle interactions with wall turbulence. *Physics of Fluids* 1996; **8**:2733–2755.
6. Li Y, Kontomaris K, McLaughlin JB. *DNS of Particle-laden Channel Flows with Feedback*. American Institute of Chemical Engineers, 1999.
7. Richter DH, Sullivan PP. Momentum transfer in a turbulent, particle-laden Couette flow. *Physics of Fluids* 2013; **25**:053304.
8. Richter DH, Sullivan PP. Sea surface drag and the role of sea spray. *Geophysical Research Letters* 2013; **40**:656–660.
9. Zhao L, Andersson HI, Gillissen JJ. Interphasial energy transfer and particle dissipation in particle-laden wall turbulence. *Journal of Fluid Mechanics* 2013; **715**:32–59.
10. Tölke J, Krafczyk M. Implementation of a lattice Boltzmann kernel using the compute unified device architecture developed by nVIDIA. *Computing and Visualization in Science* 2008; **1**:29–39.
11. Banari A, Janßen C, Grilli ST, Krafczyk M. Efficient GPGPU implementation of a lattice Boltzmann model for multiphase flows with high density ratios. *Computers and Fluids* 2014; **93**:1–17.
12. Qian YH, d’Humières D, Lallemand P. Lattice BGK models for Navier–Stokes equation. *Europhysical Letters* 1992; **17**:479–84.
13. Yu D, Mei R, Luo LS, Shyy W. Viscous flow computations with the method of lattice Boltzmann equation. *Progress in Aerospace Sciences* 2003; **39**:329–367.
14. Free surface flow simulations on GPGPUs using LBM. *Computers and Mathematics with Applications* 2011; **61**(12):3549–3563.
15. Buick J, Greated C. Gravity in lattice Boltzmann models. *Physical Review* 2000; **E61**:5307–5320.
16. Krafczyk M, Tölke J, Luo LS. Large-eddy simulations with a multiple-relaxation-time LBE model. *International Journal of Modern Physics* 2003; **B17**(01-02):33–39.
17. D’Humières D, Ginzburg I, Luo LS. Multiple relaxation time lattice Boltzmann models in three dimensions. *Philosophical Transactions Royal Society of London A* 2002; **360**:437–451.
18. Ladd AJ. Numerical simulation of particular suspensions via a discretized Boltzmann equation. Part 1. Theoretical foundation. *Journal of Fluid Mechanics* 1994; **271**:285–309.
19. Janßen C. Kinetic approaches for the simulation of non-linear free surface flow problems in civil and environmental engineering. *PhD Thesis*, Technische Universität Braunschweig, 2010.
20. Maxey MR, Riley JJ. Equation of motion for a small rigid sphere in a nonuniform flow. *Physics of Fluids* 1982; **26**:883–889.
21. Lekien F, Marsden J. Tricubic interpolation in three dimensions. *International Journal for Numerical Methods in Engineering* 2005; **63**:455–471.
22. Pope SB. *Turbulent Flows*. Cambridge University Press: Cambridge, 2000.
23. Kim J, Moin P, Moser R. Turbulence statistics in fully developed channel flow at low Reynolds number. *Journal of Fluid Mechanics* 1987; **177**:133–166.
24. Bespalko DJ. Validation of the lattice Boltzmann method for direct numerical simulations of wall-bounded turbulence. *PhD Thesis*, Queen’s University, 2011.
25. Fessler JR, Kulick JD, Eaton JK. Preferential concentration of heavy particles in a turbulent channel flow. *Physics of Fluids* 1994; **6**:3742–3749.
26. Adrian RJ. Hairpin vortex organization in wall turbulence. *Physics of Fluids* 2007; **19**:041301.
27. Zhou J, Adrian RJ, Balachandar S, Kendall TM. Mechanisms for generating coherent packets of hairpin vortices in channel flow. *Journal of Fluid Mechanics* 1999; **387**:353–396.
28. Moser R, Kim J, Mansour NN. Direct numerical simulation of turbulent channel flow up to $Re=590$. *Physics of Fluids* 1999; **11**:943–945.
29. Jeong J, Hussain F, Schoppa W, Kim J. Coherent structures near the wall in a turbulent channel flow. *Journal of Fluid Mechanics* 1997; **322**:185–214.